ELSEVIER

Journal of Structural Geology 27 (2005) 2268–2280

JOURNAL OF STRUCTURAL GEOLOGY

www.elsevier.com/locate/jsg

Microcrack networks in granite affected by a fault zone: Visualization by confocal laser scanning microscopy

Celia T. Onishi[a], Ichiko Shimizu[b,*]

[a]*Japan Nuclear Cycle Development Institute (JNC), Tono Geoscience Center, Izumi-machi, 959-31 Jyorinji, Toki-shi, Gifu 509-5102, Japan*
[b]*Department of Earth and Planetary Science, University of Tokyo, 7-3-1 Hongo, Bunkyo-ku, Tokyo 113-0033, Japan*

Received 24 June 2004; received in revised form 6 June 2005; accepted 4 July 2005
Available online 13 September 2005

Abstract

Microcracks in the Cretaceous Ryoke-type granite in Japan were investigated by using deep drilling core samples collected in the Mizunami Underground Research Project of the Japan Nuclear Cycle Development Institute (JNC). The granite body suffered brittle deformation associated with Tertiary thrust movement. Based on core-scale and microscopic deformation features, the drill core from a depth of 300 to 700 m is divided into four domains, i.e. (A) undeformed granite, (B) granite intruded by cataclastic seams, (C) fractured granite in the fault damage zone, and (D) foliated cataclasite at the fault center. To characterize microcrack geometries in each domain, we employed the impregnation method using a low-viscous acrylic resin doped with fluorescent agents and captured the microcrack images by confocal laser scanning microscopy (CLSM). The CLSM image in the fault damage zone revealed anisotropic development of microcrack networks related to the fault movement. Both CLSM observation and porosity measurements reveal a drastic increase of micro-pores in the foliated cataclasite, possibly caused by fragmentation, and granulation and crack sealing in the fault zone.

Keywords: Microcrack; Porosity; Granite; Fault; Deep drilling; Confocal laser scanning microscope (CLSM); Mizunami Underground Research Laboratory Project

1. Introduction

Transport properties of crystalline rocks are important issues in radionuclide retardation and safety management. To evaluate subsurface contamination, mechanisms of mass transport and migration pathways in crystalline rocks have been analyzed (Neretnieks, 1980; Hellmuth et al., 1993; Frieg et al., 1998; Yoshida et al., 2000). Since the diffusion rate in crystal grains is negligibly small, contaminants such as radionuclides mainly diffuse through pore water. Hence, knowledge of pore-related features such as effective porosity, connectivity, tortuosity, and permeability are necessary for hydraulic modeling and mass transport performance assessment (Moreno et al., 1997). In crystalline rocks at shallow crustal levels where brittle deformation dominates over ductile deformation, faults and fractures are considered to be the main flow paths of contaminant materials. In this study, we describe variations of fracture networks in drilling core samples of granite from intact to cataclastic rocks at the fault center.

Previous methods for the observation of fracture patterns and fluid pathways involve infiltration of liquids or viscous resin into fractured rocks. The liquid and viscous resin were marked by a colored (Baraka-Lokmane, 2002) or a fluorescent dye (Nishiyama and Kusuda, 1994, 1996), or by radioactive materials (Hellmuth et al., 1993, 1999). In the case of the fluorescent dye, fractures were highlighted by ultraviolet light. Recently, an advanced technique of the fluorescent resin impregnation method using confocal laser scanning microscopy (CLSM) was proposed by Fredrich and coworkers (Fredrich et al., 1995) and has been successfully applied to porous sedimentary rocks and crystalline rocks (Montoto et al., 1995; Fredrich and Lindquist, 1997; Fredrich, 1999; Onishi and Shimizu, 2003a,b).

One of the advantages of the CLSM is its ability to acquire the depth information, which makes it possible to construct 3D images nondestructively. The X-ray computerized tomography (CT) has also been used as a

* Corresponding author. Tel.: +81 3 5841 4513; fax: +81 3 5841 45469.
E-mail address: ichiko@eps.s.u-tokyo.ac.jp (I. Shimizu).

0191-8141/$ - see front matter © 2005 Elsevier Ltd. All rights reserved.
doi:10.1016/j.jsg.2005.07.007

nondestructive method for 3D imaging of pore structures (Montemagno and Pyrak-Nolte, 1995; Coker et al., 1996; Lindquist et al., 1996; Cislerová and Votruborvá, 2002; Wildenschild et al., 2002; Farber et al., 2003), but the typical resolution of 100 μm in medical systems is not sufficient for the imaging of micropores. Recently, the resolution has been considerably improved up to micron-orders by using synchrotron radiation (Lindquist et al., 2000; Ikeda et al., 2004). However, to obtain high-resolution X-ray CT images, the dimensions of the sample are restricted to several millimeters, which is not sufficient to characterize the fracture patterns in coarse-grained rocks such as granite. In contrast, CLSM covers a large area of sample surface with submicron resolution, while information from the interior of the samples is strongly restricted by decay of luminescent light through minerals. In this study, we characterize the microcrack networks related to fault movement by carrying the fluorescent resin impregnation method assisted by CLSM.

2. Borehole samples

In the Tono area in Gifu Prefecture, central Japan (Fig. 1), field and drilling surveys have been conducted by the Japan Nuclear Cycle Development Institute (JNC) as a case study of site characterization and performance assessment for disposal of high-level radioactive waste (Yoshida et al., 1989; Sasamoto et al., 2004). Our samples were collected from a 1014 m deep borehole site (MIU-3) at the Mizunami Underground Research Laboratory Project, located in the Shobasama-bora area of the Tono uranium mine (Toyokura et al., 2000). The MIU-3 borehole cuts the Toki granite and the Tsukiyoshi Fault at the depth (Fig. 2).

The Toki granite belongs to the Ryoke granite complex of the late Cretaceous age, which is dated to be ca. 70 Ma (Shibata and Ichihara, 1979). The granite body is composed of medium- to coarse-grained biotite–granite and biotite monzogranite, partially intruded by quartz porphyry. The Toki granite is unconformably overlain by the Tertiary sedimentary rocks composed of the Mizunami Group (15–20 Ma) and the Seto Group (0.7–5 Ma). The Toki Lignite Bearing Formation, containing uranium ore deposits, is located at the bottom of the Mizunami Group (Yusa and Yamakawa, 1992). The Toki granite and the Mizunami Group are cut by an E–W striking reverse fault of the Tsukiyoshi Fault, which dips about 70° to the south (Fig. 2).

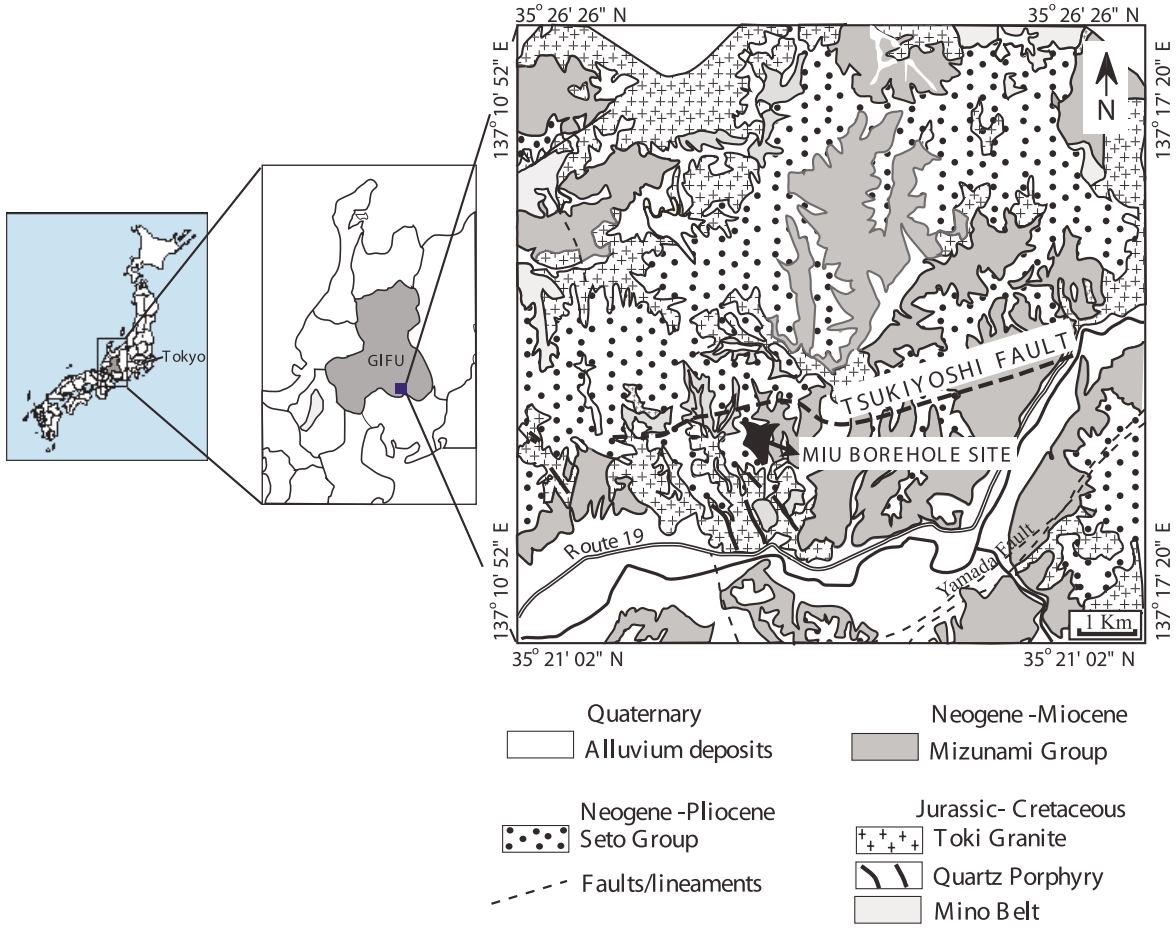

Fig. 1. A geologic map showing the distribution of the Toki granite and the location of the MIU-3 borehole site.

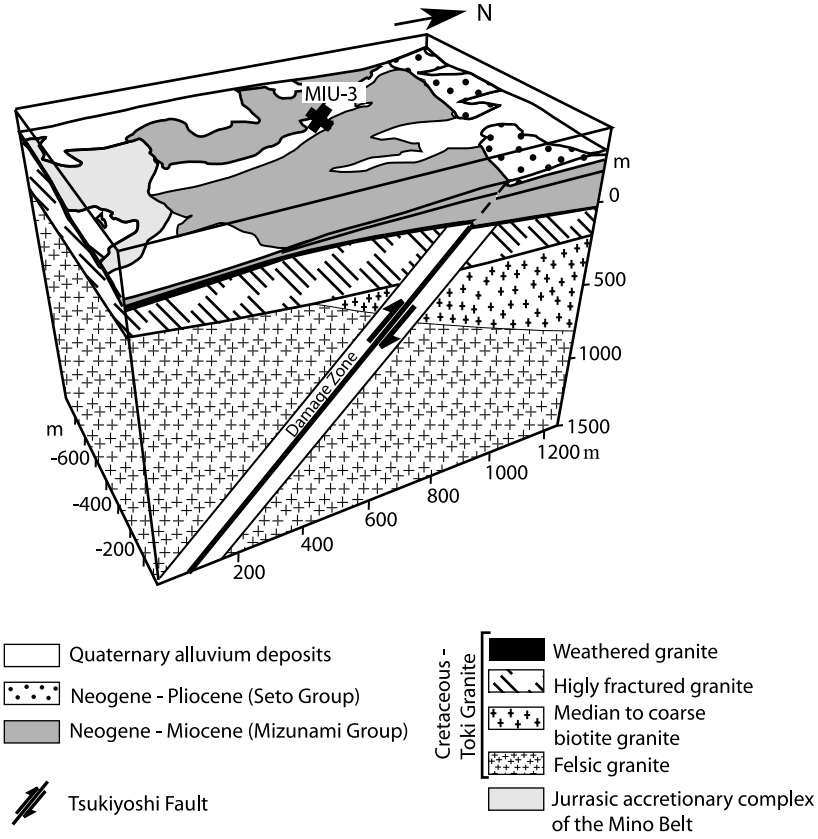

Fig. 2. A geological block model around the MIU-3 borehole site.

The vertical displacement of the fault estimated from the overlying sediments is 30 m (Toyokura et al., 2000). The Tsukiyoshi Fault is overlain by the Seto Group and thus its main activity is inferred to be late Tertiary (Itoigawa, 1974).

At the MIU-3 borehole, the granite body starts at a depth of 91.4 m from the ground surface level (Fig. 3). The borehole cuts the Tsukiyoshi Fault at a depth of 707 m. The granite core samples taken from the hanging wall of the Tsukiyoshi Fault were applied to the present analysis. All samples belong to the biotite granite, which is composed of plagioclase (20–35% in modal composition), K-feldspar (25–40%), quartz (25–35%), biotite (10–15%), and a small amount of accessory minerals such as zircon, apatite, illmenite, sericite, muscovite, epidote, and calcite. The uppermost parts of the Toki granite above 300 m are highly fractured. This fracture zone is widely recognized in borehole sites in the Tono area (Fig. 2) and, thus, is considered to be formed by weathering and thermal cracking at the margin of the plutonic body. The drill core from the uppermost fracture zone was not used in the present analysis.

Based on core-scale deformation features, together with in situ physical data from JNC, the stratigraphic column of the drilling site from a depth of about 300–707 m was divided into four domains. These are: (A) fresh undeformed granite, (B) granite intruded by cataclastic seams, (C) highly fractured granite, and (D) foliated cataclasite at the center of the Tsukiyoshi Fault (Fig. 3). Fracture planes in the host granites (Fig. 4b) are primarily developed in subvertical orientations, and foliation at the fault center dips steeply (Fig. 4d). Open cracks (mainly horizontal disking cracks) induced by stress release during core retrieval are also observed in deep cores (Fig. 4c).

For detailed analysis of microcrack networks, each core sample was cut vertically at the center. One half of the core was used for petrographic analysis for thin sections and resin impregnation, and the other half was used for porosity, pore size distribution, and permeability measurements. For microscopic analysis, vertical (V) and horizontal (H) sections were prepared for each core (Fig. 5a). When subvertical structures are developed in the core sample, the V section was cut parallel to the main fracture plane, and the H section was cut perpendicular to the V sections (Fig. 5b and c).

3. Microscopic observations

In this paper, fractures are classified as ‘intragranular’, ‘transgranular’, and ‘intergranular’. Intragranular fractures lie within a crystal grain (the cleavage microcrack in biotite is a special case of the intragranular fracture). Transgranular fractures cut across different grains. Intergranular fractures occur along grain boundaries. Under the optical microscope,

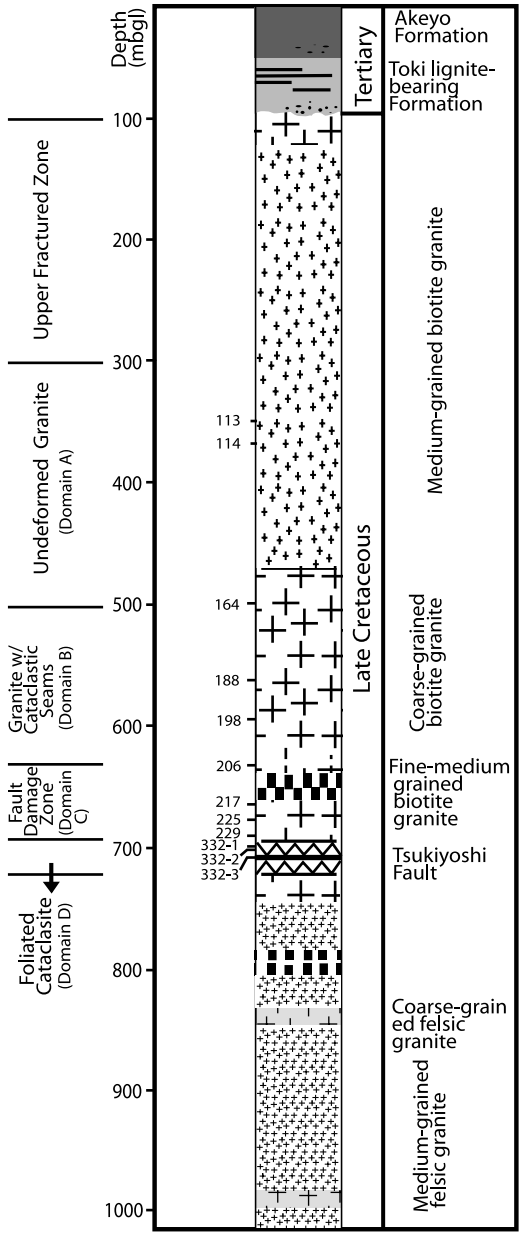

Fig. 3. A stratigraphic column at the MIU-3 borehole site. The Tsukiyoshi Fault is located at the depth of 707 m. The sample numbers are shown in the left side.

however, it is not easy to discriminate intergranular microcracks and closed grain boundaries. The resin impregnation method described later makes it possible to determine whether the grain boundary is closed or opened. In the following paragraphs, we describe microscopic features of granite in the four domains defined in the previous section.

Domain A is composed of medium-grained biotite granite with grain sizes ranging from 0.2 to 1.5 mm. Under an optical microscope, plagioclase shows albite twin and growth zoning, and partially altered at the core. K-feldspar exhibits Carlsbad twin, perthite and local mimertic structures, and is weakly altered to serecite (Fig. 6a and b). Although granite has no visible fractures in hand specimens (Fig. 4a), intragranular microcracks are found in quartz, feldspar, and biotite along the cleavage plane. Biotite is partially transformed into chlorite along the cleavage crack. Both H and V sections appear to be similar in microstructure.

Domain B consists of medium- to coarse-grained granite, with grain sizes ranging from 0.5 to 5 mm. The mineralogy is similar to that described for the undeformed granite in domain A, but in this domain the granite is sharply cut by dark green seams of various widths up to several millimeters (Fig. 4b). The dark seams, hereafter called cataclastic seams, contain fragments of quartz and feldspars sealed by a chlorite-rich matrix. The fragments show a shape preferred orientation (Fig. 6d) indicative of large displacement along the seams. Plagioclase, orthoclase and biotite show weak alteration similar to domain A. Intragranular fractures are observed in both H and V sections. Whereas cataclastic seams are primarily developed in the vertical orientation (Fig. 4b), microcrack anisotropy of wall rocks is not distinct (Fig. 6c and d).

Domain C is the upper damage zone of the Tsukiyoshi Fault, characterized by intense fracturing at the core-scale and under the microscope. The host rock is medium- to coarse-grained granite, with grain sizes ranging from 0.5 to 5 mm (Fig. 3c). Minor fault zones, which are not wider than 20 cm and occupied by fault gouge and fault breccia, are observed in some places. Microcrack anisotropy is conspicuous in this domain. H sections are characterized by development of intragranular microcracks in all directions (Fig. 6e), while parallel alignments of transgranular microcracks are developed in V sections (Fig. 6f). Although the original texture of granite is preserved, sericitization, saussuritization and chloritization are intense in all analyzed sections. A series of sections taken from this domain suggests increasing fracture density and mineral alteration toward the center of the Tsukiyoshi Fault.

Domain D is characterized by development of shear bands and overall fragmentation and grain size reduction (Fig. 3g). Grain size is highly variable and ranges from less than 0.1 to 1.5 mm. There is no clear evidence of plastic deformation and dynamic recrystallization (Fig. 6g and h) and thus the foliation is considered to be formed by cataclastic flow. Therefore, the fault rock in domain D is classified as foliated cataclasite (Chester et al., 1985). The shear bands consist of quartz–feldspathic layers and chlorite-rich ultracataclastic layers, including fragments of feldspars in the fine-grained matrix of quartz, feldspar and clay minerals. The clay minerals identified by X-ray diffractometry (XRD) are chlorite and smectite, and a small amount of vermiculite and/or halloysite. Calcite veins are concentrated at the margins of the fault zone.

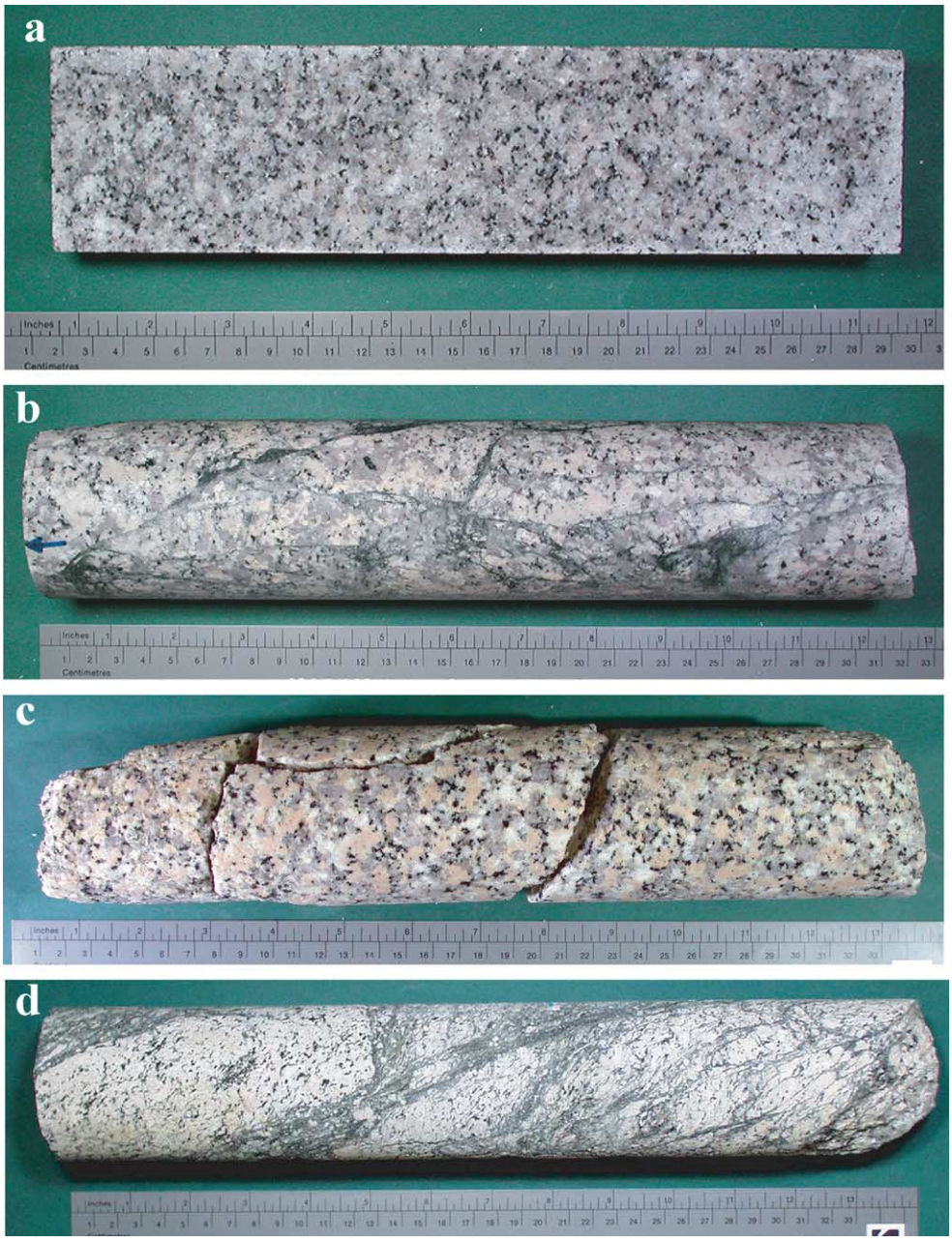

Fig. 4. Examples of the drill core samples. (a) Fresh and undeformed granite in domain A. Sample 113, depth 350 m from the ground surface. (b) Fractured granite in domain B intruded by cataclastic seams. Sample 188, depth 575 m. (c) Fractured granite in the fault damage zone of domain C. Sample 229, depth 698 m. (d) Foliated cataclasite in domain D at the center of the Tsukiyoshi Fault. Sample 332, depth 707 m.

4. Porosity and pore size distribution

Porosity was measured by a helium pycnometer and by the mercury-injection method. The former, using compressible helium gas, efficiently measures the bulk porosity of low-porosity rocks. Rectangular samples of $2\times2\times5$ cm^3 were oven dried for 24 h and measured by an Ultrapore-300 Helium Pycnometer (Core Laboratories Instrument).

The mercury-injection method allows us to estimate pore-size distribution as well as bulk porosity. The pore size distribution is determined from the volumes of liquid mercury intruded into the pore spaces at elevated injection pressure. We prepared two cubic $1\times1\times1$ cm^3 samples for each drill core sample. The samples were pre-dried and measured by Auto Pore III 9420 (MICROMERITICS). Assuming tubular shapes of micro-pores, the equivalent pore diameter (D) was calculated. The maximum pressure applied by the apparatus was 400 MPa, which corresponds to the equivalent pore diameter of the order 0.001 μm. It should be noted that the mercury injection method might underestimate the volume of small pores due to the presence

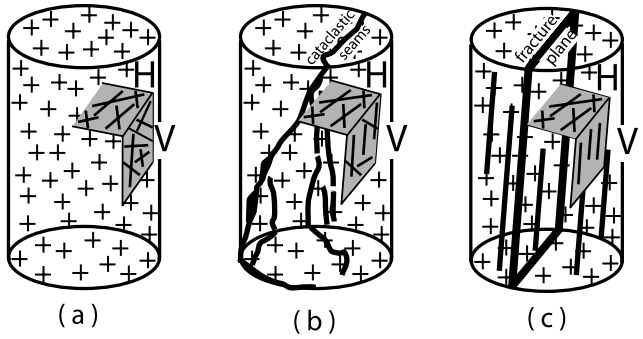

Fig. 5. Schematic illustrations of borehole cores showing the orientations of mutually orthogonal sections. (a) Undeformed granite in domain A. (b) Granite intruded by cataclastic seams. (c) Fractured granite and foliated cataclasite in domain C and D.

of bottleneck or dead-end pores, and/or overestimate the volume of large pores due to deformation by injection pressure.

Fig. 7 shows the bulk porosities of each sample measured by these two methods. The bulk porosity ranges from 0.5 to 3.5% in fresh granites and fractured granites in domains A, B, and C, but increases up to 8% in the foliated cataclasite at the fault center in domain D. Fig. 8 shows cumulative pore volumes and pore size distributions. Undeformed granite in domain A and deformed granites in domains B and C have bimodal or multimodal pore size distributions (Fig. 8a–c). At the fault zone, the pore size distribution changes to a unimodal one with the maximum pore size around 1 μm (Fig. 8d).

5. Visualization of microcracks by laser scanning microscopy

For visualization of fluid pathways in fractured rocks, the fluorescent resin impregnation has been performed in both fields (Chen et al., 1996; Frieg et al., 1998; Ota et al., 1998; Yoshida et al., 2000; Schild et al., 2001) and laboratories (Nishiyama and Kusuda, 1994, 1996). For observation of microcracks, a fluorescent microscope (or alternatively, an ordinary microscope with an ultraviolet light source) had been used. CLSM is a relatively new technique and has been applied to the resin impregnation method in recent years (Fredrich et al., 1995; Montoto et al., 1995; Fredrich and Lindquist, 1997; Fredrich, 1999). Because of the use of narrow laser beams instead of a point light source, clear and non-scattered images can be observed under CLSM. Moreover, since optical images distant from the focal plane are shut out in the confocal optical path, high-contrast images can be obtained (e.g. fig. 2 of Montoto et al. (1995)). In addition to these optical advantages, CLSM enables us to capture a digital intensity map of fluorescent light. Hence, image qualities such as brightness and contrast can be rather easily improved by digital image processing. We applied CLSM for characterization of microcrack networks in the Toki granite.

5.1. Apparatus

We used a laser scanning microscope FLUOVIEW (OLYMPUS Co.) installed in the Division of Earth and Planetary Science, University of Tokyo. The CLSM is equipped with a Kr–Ar laser source with wavelengths (λ) of 488, 568, and 647 nm. In this study, a high-pass filter is used to cut reflected light and detect fluorescence excited by blue laser ($\lambda = 488$ nm). Granite-forming minerals exhibit no fluorescence at this wavelength. The fluorescent light is detected by a photomultiplier tube (PMT), and is transformed to 12-bit (i.e. 4096 gray level) digital data. By scanning laser beams over a sample in x and y directions, we can obtain a digital intensity map of fluorescent light. The size of the digital image in FLUOVIEW is 1024×1024 pixels at maximum, and was usually scanned within 1 min. The z-scan is performed by the movement of sample stage actuated by a motor. The minimum step size in the z-axis is 0.1 μm. Details of the system are described by Shimizu and Shimada (2002).

In general, spatial resolution of optical microscopes depends on the wavelength of the light source and numerical aperture (NA) of the objective lens. The theoretical limit of the Raileigh resolution for an ordinary optical microscope is given as:

$$Fxy = 0.61\lambda/\mathrm{NA}. \quad (1)$$

In the case of CLSM, the optical resolution is improved by the use of coherent laser beams and the confocal optical path. In the fluorescent mode, the Raileigh resolution of CLSM is expressed as:

$$Fxy = 0.46\ \lambda/\mathrm{NA}. \quad (2)$$

A vertical resolution can also be defined for the CLSM, which is given by a half-width value in the z-direction as:

$$Fz = 1.28\ n\lambda/\mathrm{NA}^2. \quad (3)$$

Here, n is the refractive index of the matrix (air or immersion oil). Generally, an objective lens with high magnification has a large NA number. By the use of a high-magnification lens (OLYMPUS UplanApo 100× Oil, NA 1.4), optical resolutions up to $Fxy = 0.16$ μm and $Fz = 0.48$ μm are realized in our system, but the sample area covered by a single x–y scan is limited, in this case, to 141×141 μm^2. To figure out the connectivity and orientations of microcrack networks in granite samples, we used relatively low magnification lens (OLYMPUS Uplan Apo 10×, NA 0.3) for the present study. As a result, the theoretical limit of optical resolution for the Kr–Ar blue laser ($\lambda = 488$ nm) becomes 0.75 μm for x and y directions and 6.94 μm for the z direction.

Optical resolution in the actual system is considered to be

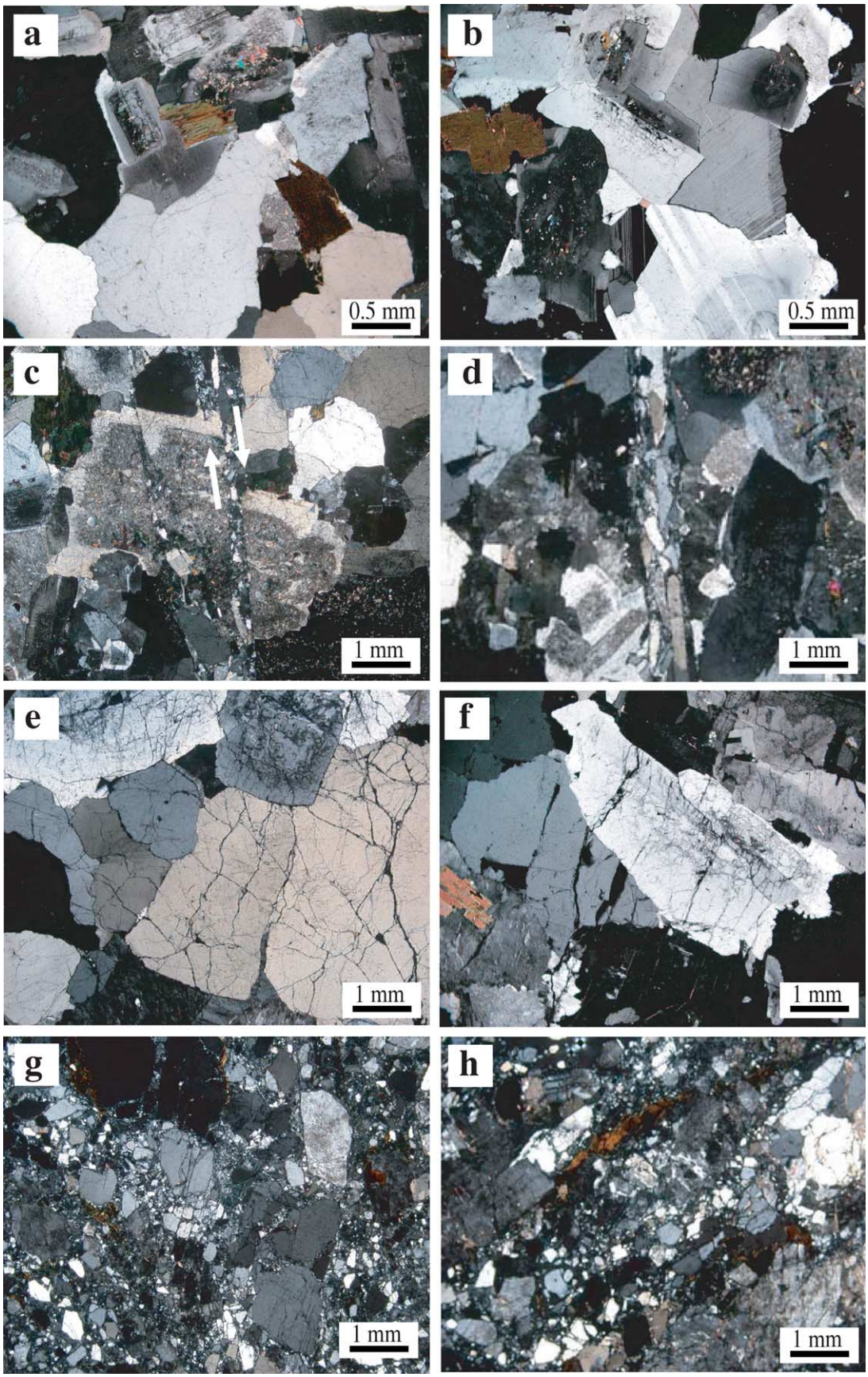

Fig. 6. Microphotographs of the Toki granite in H sections ((a), (c) and (e)) and V sections ((b), (d) and (f)) under cross-polarized light. (a) and (b) Undeformed granite in domain A. Sample 113. (c) and (d) Fractured granite in domain B. Note the displacement of a plagioclase grain along a small-scale cataclastic seam. Arrows show apparent displacement. Sample 188. (c) Highly fractured granite in domain C. Sample 229. (d) Foliated cataclasite in domain D. Sample 332.

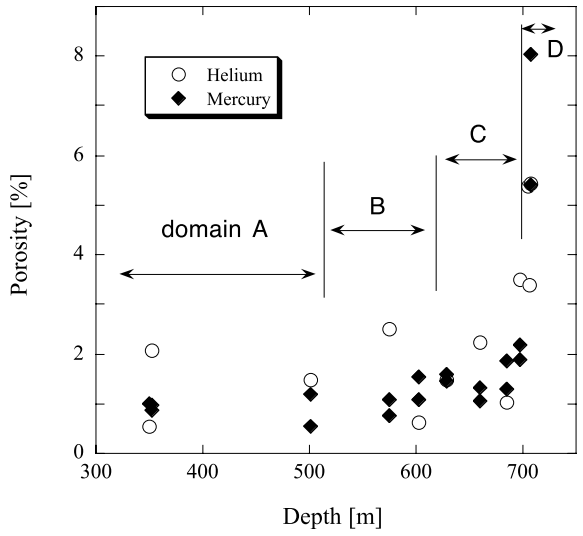

Fig. 7. Variations of bulk porosity with depth measured by a helium pycnometer and the mercury injection method.

larger than the above-mentioned values, because aperture of a confocal pin-hole (i.e. confocal apertures, CA) and diameters of laser beams have finite values. Smaller CA is desirable for better resolution, but the intensity of fluorescent light becomes weak (Fredrich, 1999). Brightness of CLSM images is also affected by laser intensity and gain of PMT. High laser intensity and gains of PMT are favorable for obtaining bright images, but the noise is increased at the same time. These parameters were determined so that the quality of the images is optimized.

The scan area for a single x–y image was chosen to be 1414×1414 μm^2. Consequently, the pixel resolution (or a skip size) of an x–y image with the size of 1024×1024 pixels becomes 1.38 μm^2. Because the pixel resolution is larger than the optical resolution of 0.75 μm, the actual resolution of x–y images is constrained by the former. The vertical step in the z-direction was taken to be 0.5 μm. This is much smaller than 6.94 μm and, thus, does not affect the optical resolution Fz.

5.2. Resin impregnation

In the fluorescent method, epoxy (Fredrich, 1999) and acrylic resins such as methylmetacrylate and cyanoacrylate (Nishiyama and Kusuda, 1994; Frieg et al., 1998; Schild et al., 2001) pre-mixed with fluorescent agents have been used. We used methylmetacrylate with a viscosity lower than 1.5 (mPa s), which is similar to the viscosity of water. Before the impregnation of the resin, coupon samples of the size of $40 \times 25 \times 25$ mm^3 were dried for 48 h at a temperature of 85–90 °C. Each sample was then soaked in a container filled with the resin and left under vacuum until degassing ceased, indicating complete impregnation of the resin into the rock matrix. This step usually requires several hours. The pressure was then slowly released to the atmospheric level. The samples were heated to 80 °C in a water bath, and after complete hardening of the resin, were cut at the center and polished to make thin sections. To acquire the depth (x–z) profiles, the thin sections were made thicker (>150 μm) than those used for standard petrographic analysis.

5.3. Image acquisition and image processing

For each coupon sample, we scanned 10 optical slices near the sample surface, using 2 μm vertical steps. A lateral (x–y) image was constructed by stacking these 10 optical slices. This procedure was applied to avoid the effects of surface irregularities. In the depth profiles, z-scale is usually limited to 200–250 μm since fluorescence from the interior of rock samples decay due to absorbance in silicate minerals. The quality of digitized fracture images captured by CLSM was improved by digital image processing using commercial software, which can handle 12-bit data. The Gaussian and median filters were applied to reduce noise (Gonzalez and Woods, 2001). The examples of microcrack images visualized by CLSM are shown in Fig. 9. Relative intensity of fluorescent light after these operations is represented by pseudocolors.

Fredrich and co-workers (Fredrich and Lindquist, 1997; O'Connor and Fredrich, 1999) have utilized the CLSM images for quantification of pores in porous sandstones. In principle, porosity can be measured by counting the number of pixels (or voxels for 3D images) occupied within the pores. For this procedure, pore distribution should be visualized as a 'black and white' image but the pore images actually acquired by the CLSM have a certain intensity variation. Therefore, a threshold needs to be determined to filter noise and transform digitized images from gray-scale to binary. In the present case of granite, however, the threshold was not well defined due to two primary reasons (Onishi and Shimizu, 2003b). (1) Intermediate intensities in the fluorescent images are mainly due to the presence of tiny cracks in granite. As clarified by the mercury injection method (Fig. 8), large numbers of cracks have submicron pores, which are smaller than the pixel resolution of 1.38 μm^2. Sub-pixel cracks would have been detected as a material with weak fluorescence. (2) Moreover, since we used a low magnification (and low NA) objective lens, vertical resolution of 6.94 μm was much larger than the lateral resolution of 1.38 μm^2. Therefore, fluorescence at the depth considerably overlaps the x–y images (Fig. 9). Because these two effects are serious for non-porous crystalline rocks, the CLSM images were not used for quantitative analysis of porosity, but only for characterization of microcracks.

5.4. Characterization of microcrack geometries

In undeformed granite (domain A), most grain boundaries are filled with the fluorescent resin (Fig. 9a). The grain

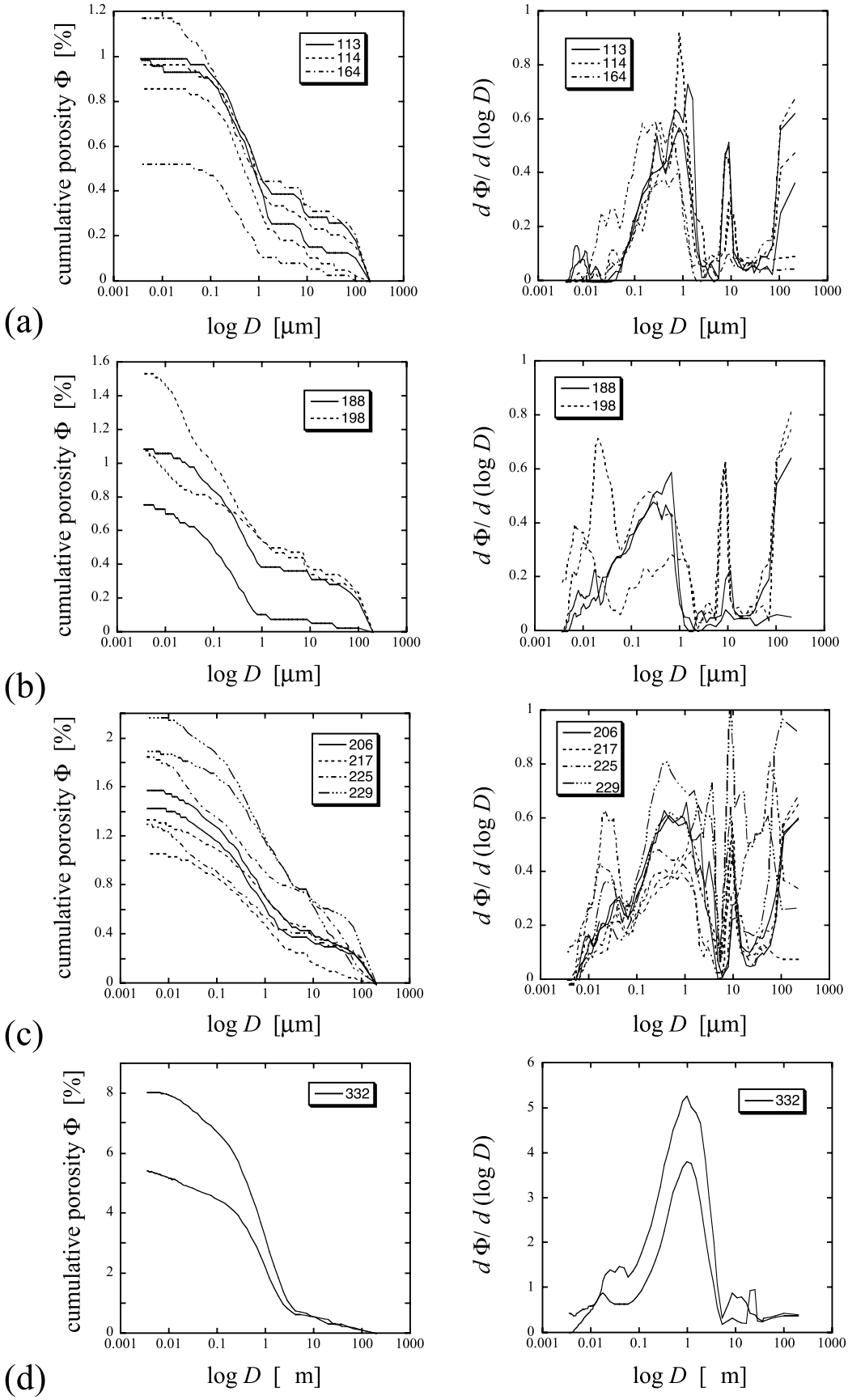

Fig. 8. Cumulative porosities Φ (left) and pore size distributions (right) measured during elevated injection pressure of mercury (i.e. decreasing pore diameter *D*). (a) Domain A, (b) Domain B, (c) Domain C, (d) Domain D.

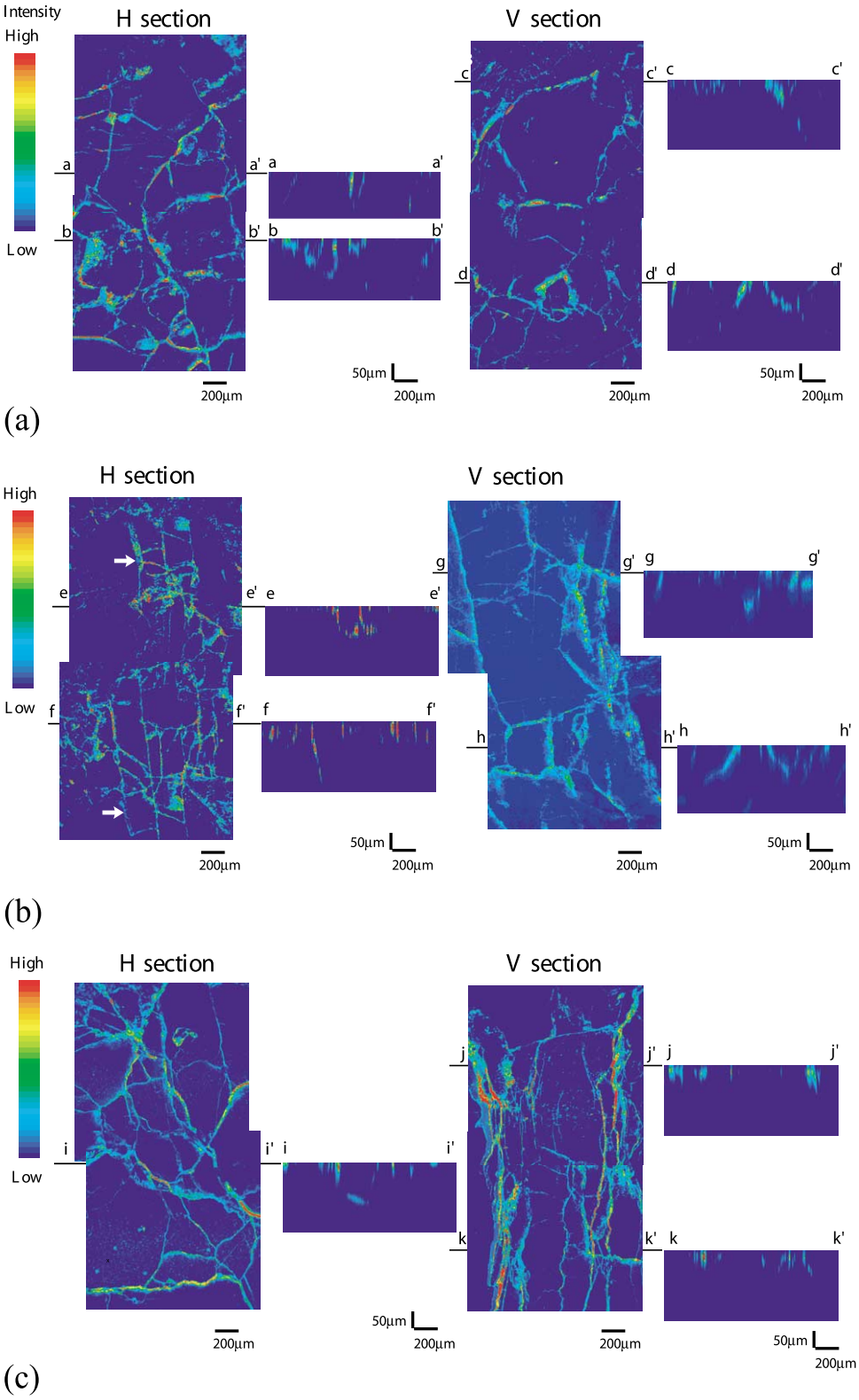

Fig. 9. Microcrack images of the Toki granite visualized by the combination of the fluorescent resin impregnation method and confocal laser microscopy (CLSM). Relative intensity of fluorescent light is represented by pseudocolor. The depth (x–z) profiles are shown to the right of the lateral (x–y) images. Note that the vertical (z) scale is exaggerated in the depth profiles. (a) Undeformed granite in domain A. Sample 113. (b) Fractured granite in domain B. Arrows indicate cataclastic seams. Sample 188. (c) Highly fractured granite in domain C. Sample 229. (d) Foliated cataclasite in domain D. Sample 332. See text for details.

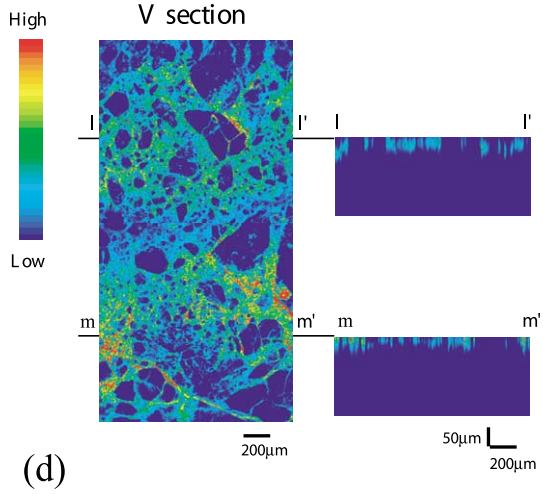

Fig. 9 (*continued*)

boundary (or intergranular) microcracks and intragranular microcracks formed interconnected networks in both H and V sections. Similarly in domain B, the microcracks are observed at grain boundaries and along the wall of the cataclastic seams in both H and V sections (Fig. 9b). In domains A and B, there are no distinct differences in microcrack distribution between H and V sections.

In the fault damage zone (domain C), H and V sections show different features under CLSM (Fig. 9c). In H sections, intergranular and intragranular microcracks oriented in various directions are interconnected and form anastomosing networks. In contrast, V sections have transgranular fractures that are aligned sub-vertically and intergranular microcracks are also observed. In domain D, at the center of Tsukiyoshi Fault, no microcrack anisotropy is recognized due to overall fragmentation and grain size reduction. The fluorescent resin is highly concentrated in the fine-grained matrix (Fig. 9d). In the x–z profiles, fluorescent light is detected only at the shallow part of the coupon samples. This may be possibly due to high concentrations of colored minerals such as chlorite and the resin itself, which prevent transmission of laser beams from the sample surface and fluorescent light from the sample depth.

6. Discussion

We have measured the bulk porosity of samples by two different methods using helium gas and mercury injection. Although both methods give connected (or effective) porosity of the samples, lower values may be expected for the mercury injection method because of higher viscosity of liquid mercury as compared to helium gas. In addition, if the sample size effect was significant, larger cracks may have been overlooked in the mercury injection method because the dimensions of the samples were smaller. Nevertheless, the data show no systematic difference between the two methods. The results of porosity measurements shown in Fig. 7 indicate that, beyond the measurement errors and sample heterogeneity, there is a distinct difference between host granites of domains A, B, C, and the main fault zone in domain D. The porosity in the former ranges from 1 to 2%, whereas that in the latter exceeds 5%. The abrupt increase in porosity is also confirmed by the CLSM images (Fig. 9d). The porosity of undeformed granites in the Toki granite is similar to those reported in other granitic bodies (Brace et al., 1968; Kiyama et al., 1996; Morrow and Locker, 1997; Yoshida et al., 2000). The relationship between fault structures and porosity revealed here is similar to those described by Caine et al. (1996), Evans et al. (1997), Geraud et al. (1995), and Seront et al. (1998).

In the Toki granite, the increase in porosity is associated with the change in pore size distribution. Host granites show bimodal or multimodal distributions (Fig. 8a–c). Peaks around 1 μm exist in all samples in domains A, B, and C, and are possibly attributed to grain boundary pores. Peaks around 10 and 100 μm exist in many samples, but microcracks with the width over 100 μm were rarely observed by CLSM. It is possible that these largest 'pores' represent surface roughness of the sample cubes. Compared with undeformed granite (Fig. 8a), pore size distributions become scattered and variable in deformed granite in domains B and C (Fig. 8b and c). Some samples have peaks at submicron pores and others do not. These peaks might represent individual cataclastic zones contained in the sample cube since the size of sample cubes is comparatively small. At the fault zone (Fig. 8d) the volume fraction of micron-sized pores becomes large with respect to larger pores. This is probably due to the breakdown of larger pore spaces and filling of fragmented materials, and precipitation of fine-grained minerals such as chlorite in the course of hydrothermal alteration.

The CLSM images of the Toki granite have clarified the variation of microcrack geometries from the host granite to the main fault zone. In relatively shallow parts of the drill core (domains A and B), no fracture anisotropy is recognized at microscopic scales, although at the core-scale, millimeter-sized cataclastic seams have a tendency to develop in the vertical orientation (Fig. 4b). Randomly oriented microcracks might be introduced by thermo-elastic effects during cooling of granite and by stress release during emplacement of the plutonic body. Relaxation during core retrieval and sample preparations possibly enhanced propagation of pre-existing microcracks.

Granite in the fault damage zone (domain C) is characterized by anastomosing fracture networks in H sections, and parallel alignment of microcracks in V sections. Dominance of vertical microcracks is inferred from these orthogonal sections. Because vertical microcracks are sub-parallel to the main fault plane of the Tsukiyoshi Fault, their formation is most likely explained by the fault movement. Although cracking by stress relaxation becomes significant in deep drilling cores, unloading cracks tend to develop in the horizontal direction

(as seen in core disking in Fig. 2c) and are not considered as a main cause of the vertically oriented microcracks. At the fault center, composed of foliated cataclasite (domain D), anisotropic fabrics are distinct in the core samples (Fig. 4d), although the internal structures of the ultracataclasite bands are rather isotropic (Fig. 9d).

From the distinct change in porosity clarified in this study, focused fluid flow along the fault zone might be expected as demonstrated in other fault zones (Caine and Forster, 1999). However, permeability of fluids is not determined by a single parameter of porosity but by combined effects of crack density, crack width, and connectivity of fracture networks. Although the bulk porosities are small in host granites, most grain boundaries are open and connected with intragranular microcracks. Therefore, diffuse flow along inter- and intragranular microcracks would also be important. It should be noted that the porosity and pore structures might have been altered during extraction of the drilling core or during sample preparation with mercury injection and/or resin impregnation under vacuum. Schild et al. (2001) have shown in their in situ impregnation samples that the porosity measured by conventional laboratory methods was 2–2.5 times higher than the original values. More detailed studies are needed to clarify transport properties of the Toki granite at the depth where this study was conducted. For this purpose, we have performed permeability measurements on the present core samples at high confining pressure. The result of the measurements and its relation to the present observations on microcrack geometries will be detailed in a future paper.

7. Conclusions

We investigated deep drilling core samples of the Toki granite to examine deformation features and fluid pathways in granite affected by late Tertiary fault movements. Microcracks patterns were investigated by ordinary petrographic analysis using a polarized microscope, and further by CLSM. In the latter case, pore spaces were identified by a low-viscous resin of methylmetacrylate doped with fluorescent dye. Microcrack patterns visualized by CLSM were compared with the results of petrophysical analysis on porosity and pore-size distributions. The main findings are as follows:

(1) Except for the cover sediments and highly fractured granites near the ground surface, the drilling core is divided into four domains (denoted as A, B, C, and D from a depth of 300 m to the main fault zone at 700 m) based on deformation features in the mesoscopic and microscopic scales. Domain A consists of fresh biotite granite. Granite in domain B is characterized by intrusion of cataclastic seams. In domain C, granite is highly fractured in the hanging wall of the fault plane. Domain D is the center of the fault zone constituting foliated cataclasite.
(2) In the host granites in domains A, B, and C, microcracks were observed along grain boundaries and within crystal grains. In fractured granites in domain C, microcracks have a strong tendency to align in the subvertical orientation. Foliation at the main fault zone (domain D) is also subvertical. It is possible that microcrack anisotropy in domain C is related to the fault movement.
(3) Foliated cataclasite in domain D exhibits fragmentation, grain size reduction, and precipitation of chlorite by hydrothermal alteration, which results in the generation of submicron pores and a drastic increase in porosity (over 5%) in the fault zone.

Acknowledgements

We acknowledge Joanne T. Fredrich and Axel Vollbrecht for detailed reviews and constructive comments. We thank Glen McCrank, Kazuhiro Hama, Kenji Amano, Kunio Ota, Takashi Ando, Hiromi Hayashi, and Eiji Sasao for discussions and technical support. We also thank Liviu Tomutsa and Marcelo Lippmann for an earlier English version of the manuscript. This work was supported by post-doctoral fellowship of the Japan Nuclear Cycle Development Institute (JNC).

References

Baraka-Lokmane, S., 2002. A new resin impregnation technique for characterizing fracture geometry in sandstone cores. International Journal of Rock Mechanics and Mining Sciences 39, 815–823.

Brace, W.F., Walsh, J.B., Frangos, W.T., 1968. Permeability of granite under high pressure. Journal of Geophysical Research 73, 2225–2236.

Caine, J.S., Forster, C.B., 1999. Fault zone architecture and fluid flow: insights from field data and numerical modeling. In: Haneberg, W., Mozley, P.S., Moore, J.C., Goodwin, L.B. (Eds.), Faults and Subsurface Fluid Flow in the Shallow Crust. American Geophysical Union Monograph 113, pp. 101–127.

Caine, J.S., Evans, J.P., Forster, C.B., 1996. Fault zone architecture and permeability structure. Geology 24, 1025–1028.

Chen, Y., Nishiyama, T., Terada, M., Iwamoto, Y., 1996. A fluorescent approach to the identification of grout injected into fissures and pore spaces. Engineering Geology 43, 395–401.

Chester, F.M., Friedman, M., Logan, J.M. 1985 Foliated cataclasites, Tectonophysics. 111, 139–146.

Císlerová, M., Votruborvá, J., 2002. CT derived porosity distribution and flow domains. Journal of Hydrology 267, 186–200.

Coker, D.A., Torquato, S., Dunsmuir, J.H., 1996. Morphology and physical properties of Fontainebleau sandstone via a tomographic analysis. Journal of Geophysical Research 101, 17497–17506.

Evans, J.P., Forster, C.B., Goddard, J.V., 1997. Permeability of fault-related rocks, and implications for hydraulic structure of fault zones. Journal of Structural Geology 19, 1393–1404.

Farber, L., Tardos, G., Michels, J.N., 2003. Use of X-ray tomography to study the porosity and morphology of granules. Powder Technology 132, 57–63.

Fredrich, J.T., 1999. 3D imaging of porous media using laser scanning confocal microscopy with application to microscale transport processes. Physics and Chemistry of the Earth 24, 551–561.

Fredrich, J.T., Lindquist, W.B., 1997. Statistical characterization of the three-dimensional microgeometry of porous media and correlation with microscopic transport properties. International Journal of Rock Mechanics and Mining Sciences 34, 3–4.

Fredrich, J.T., Menendez, B., Wong, T.-F., 1995. Imaging the pore structure of geomaterials. Science 268, 276–279.

Frieg, B., Alexander, W.R., Bühler, C., Haag, P., Möri, A., Ota, K., 1998. In situ resin impregnation for investigating radionuclide retardation in fractured repository host rocks. Journal of Contaminant Hydrology 35, 115–130.

Geraud, Y., Caron, J.M., Faure, P., 1995. Porosity network of a ductile shear zone. Journal of Structural Geology 17, 1757–1769.

Gonzalez, R.C., Woods, R.E., 2001. Digital Image Processing. Prentice Hall, Upper Saddle River, New Jersey. 793pp.

Hellmuth, K.H., Siitari-Kauppi, M., Lindberg, A., 1993. Study of porosity and migration pathways in crystalline rock by impregnation with ^{14}C-polymethylmethacrylate. Journal of Contaminant Hydrology 13, 403–418.

Hellmuth, K.H., Siitari-Kauppi, M., Klobes, P., Meyer, K., Goebbels, J., 1999. Imaging and analyzing rock porosity by autoradiography and Hg-porosimetry/X-ray computer tomography—applications. Physics and Chemistry of the Earth 27, 569–573.

Ikeda, S., Nakano, T., Tsuchiyama, A., Uesugi, K., Suzuki, Y., Nakamura, K., Nakashima, Y., Yoshida, H., 2004. Nondestructive three-dimensional element-concentration mapping of a Cs-doped partially molten granite by X-ray computed tomography using synchrotron radiation. American Mineralogist 89, 1304–1312.

Itoigawa, J., 1974. Seto Group, Monograph of the Mizunami Fossil Museum, No. 1 1974, pp. 373–384 (in Japanese).

Kiyama, T., Kita, H., Ishijima, Y., Yanagidani, T., Aoki, K., Sato, T., 1996. Permeability in anisotropic granite under hydrostatic compression and triaxial compression including post-failure region. North America Rock Mechanics Symposium, 1161–1168.

Lindquist, W.B., Lee, S.M., Coker, D.A., Jones, K.W., Spanne, P., 1996. Medial axis analysis of three dimensional tomographic images of drill core samples. Journal of Geophysical Research 101, 8297–8310.

Lindquist, W.B., Venkatarangan, A., Dunsmuir, J., Wong, T.-F., 2000. Pore and throat size distribution measured from synchrotron X-ray tomography images of Fontainebleau sandstones. Journal of Geophysical Research 105, 21509–21527.

Montemagno, C.D., Pyrak-Nolte, L.J., 1995. Porosity of natural fracture networks. Geophysical Research Letters 22, 1397–1400.

Montoto, M., Martinez-Nistal, A., Rodriguez-Rey, A., Fernando-Merayo, N., Soriano, P., 1995. Microfractography of granite rocks under confocal scanning laser microscopy. Journal of Microscopy 177, 138–149.

Moreno, L., Gylling, B., Neretnieks, I., 1997. Solute transport in fractured media—the important mechanisms for performance assessment. Journal of Contaminant Hydrology 25, 283–298.

Morrow, C.A., Locker, D.A., 1997. Permeability and porosity of the Illinois UHP3 drillhole granite and a comparison with other deep drillhole rocks. Journal of Geophysical Research 102, 3067–3075.

Neretnieks, I., 1980. Diffusion in the rock matrix: an important factor in radionuclide retardation? Journal of Geophysical Research. 85, 4379–4397.

Nishiyama, T., Kusuda, H., 1994. Identification of pore space and microcracks using fluorescent resins. International Journal of Rock Mechanics and Mining Sciences & Geomechanical Abstract 31, 369–375.

Nishiyama, T., Kusuda, H., 1996. Application of a fluorescent technique to the study of the weathering process. Engineering Geology 43, 247–253.

O'Connor, R.M., Fredrich, J.T., 1999. Microscale flow modeling in geologic materials. Physics and Chemistry of Earth 24, 611–616.

Onishi, C.T., Shimizu, I., 2003a. Visualization of microcracks in granite using a laser scanning microscope. Journal of Geological Society of Japan 109, XIX–XX (in Japanese).

Onishi, C.T., Shimizu, I., 2003b. Imaging of microcracks in granite by a fluorescent method assisted by laser scanning microscope (LSM). Journal of Geological Society of Japan 109, 607–610 (in Japanese).

Ota, K., Amano, K., Ando, T., 1998. Brief overview of in situ contaminant retardation in fractured crystalline rock at Kamaishi in situ test site. Proceedings of International Workshop for the Kamaishi In Situ Experiments. Japan Nuclear Cycle Development Institute, Tokai-mura, Ibaraki-ken, Japan, pp. 67–76.

Sasamoto, H., Yui, M., Arthur, R.C., 2004. Hydrochemical characteristics and groundwater evolution modeling in sedimentary rocks of the Tono mine, Japan. Physics and Chemistry of the Earth 29, 43–54.

Schild, M., Shiegesmund, S., Vollbrecht, A., Mazurek, M., 2001. Characterization of granite matrix porosity and pore-space geometry by in situ and laboratory method. Geophysical Journal International 146, 111–125.

Seront, B., Wong, T.-F., Caine, J.S., Forster, C.B., Bruhn, R.L., 1998. Laboratory characterization of hydromechanical properties of a seismogenic normal fault system. Journal of Structural Geology 20, 865–881.

Shibata, K., Ishihara, S., 1979. Rb–Sr whole-rock and K–Ar mineral ages of granitic rocks of the Komagane district, Nagano Prefecture, central Japan. Geochemical Journal 13, 113–119.

Shimizu, I., Shimada, K., 2002. Development of a polarized laser scanning microscope and its use to quantitative analysis of rock textures. Journal of Geological Society of Japan 108, 306–317 (in Japanese with English abstract).

Toyokura, I., Hashii, T., Nagoe, S., Ito, T., Sugimori, T., Sugita, N.. Masaeda, H., 2000. Drilling survey (MIU-3) of Mizunami Underground Research Laboratory Project in Shomasama-bora site. JNC Technical Report, JNC TJ7440 2000-022, Japan Nuclear Cycle Development Institute, 1520 pp. (in Japanese with English abstract).

Wildenschild, D., Hopmans, J.W., Vaz, C.M.P., Rivers, M.L., Rikard, D., Christensen, B.S.B., 2002. Using X-ray computed tomography in hydrology: systems, resolutions, and limitations. Journal of Hydrology 267, 285–297.

Yoshida, H., Ohsawa, H., Yanagizawa, K., Yamakawa, M., 1989. Analysis of fracture system in granitic rocks—case study for the granitic rock, Gifu Prefecture, Japan. Journal of Japan Society of Engineering Geology 30, 11–22 (in Japanese with English abstract).

Yoshida, H., Aoki, K., Semba, T., Ota, K., Amano, K., Hama, K., Kawamura, M., Tsubota, K., 2000. Overview of the stability and barrier functions on the granite geosphere at the Kamaishi Mine: relevance to radioactive waste disposal in Japan. Engineering Geology 56, 151–162.

Yusa, Y., Yamakawa, M., 1992. Tono in situ research facilities for studies of the geological environment. Guidebook of 29th IGc Field Trip B18, pp. 145–153.